

# SPARC: Accurate and efficient finite-difference formulation and parallel implementation of Density Functional Theory. Part II: Periodic systems

Swarnava Ghosh<sup>a</sup>, Phanish Suryanarayana<sup>\*,a</sup>

<sup>a</sup>*College of Engineering, Georgia Institute of Technology, GA 30332, USA*

---

## Abstract

As the second component of SPARC (Simulation Package for Ab-initio Real-space Calculations), we present an accurate and efficient finite-difference formulation and parallel implementation of Density Functional Theory (DFT) for periodic systems. Specifically, employing a local formulation of the electrostatics, the Chebyshev polynomial filtered self-consistent field iteration, and a reformulation of the non-local force component, we develop a finite-difference framework wherein both the energy and atomic forces can be efficiently calculated to within chemical accuracies. We demonstrate using a wide variety of materials systems that SPARC obtains high convergence rates in energy and forces with respect to spatial discretization to reference plane-wave result; energies and forces that are consistent and display negligible ‘egg-box’ effect; and accurate ground-state properties. We also demonstrate that the weak and strong scaling behavior of SPARC is similar to well-established and optimized plane-wave implementations for systems consisting up to thousands of electrons, but with a significantly reduced prefactor. Overall, SPARC represents an attractive alternative to plane-wave codes for performing periodic DFT simulations.

**Key words:** Electronic structure, Real-space, Finite-differences, Electrostatics, Atomic forces, Parallel computing

---

## 1. Introduction

Density Functional Theory (DFT) developed by Hohenberg, Kohn, and Sham [1, 2] is a popular ab-initio method for understanding as well as predicting a wide range of materials properties [3, 4, 5, 6]. However, the solution of the DFT problem still remains a formidable task, which severely restricts the size of systems that can be studied. The choice of a plane-wave discretization [7, 8, 9, 10, 11, 12] is attractive since it forms a complete and orthonormal set, provides spectral convergence with increasing basis size, enables the efficient evaluation of convolutions through the Fast Fourier Transform (FFT) [13], and is amenable to efficient and effective preconditioning [14, 15]. However, the need for periodicity makes the plane-wave basis unsuitable for the study of non-periodic and localized systems such as isolated clusters and crystal defects [16, 17, 18]. Additionally, its non-local nature makes the efficient use of modern large-scale computer architectures particularly challenging [19, 20], and the development of methods that scale linearly with respect to the number of atoms impractical [21, 22].

The aforementioned limitations of the plane-wave basis have motivated the development of various real-space DFT implementations, including finite-differences [23, 24, 25, 26, 27], finite-elements [28, 29, 30, 31, 32, 33], wavelets [34, 35, 36], periodic sinc functions [37], basis splines (B-splines) [38], non-uniform

---

<sup>\*</sup>Corresponding Author ([phanish.suryanarayana@ce.gatech.edu](mailto:phanish.suryanarayana@ce.gatech.edu))

rational B-splines (NURBS) [39], and maximum entropy basis functions [40]. However, despite the success of real-space approaches, plane-wave implementations still remain the method of choice for practical DFT computations. This is mainly due to their superior performance in achieving chemical accuracies on the modest computational resources that are commonly available to researchers.

The finite-difference discretization is an attractive option for performing real-space DFT simulations because it results in a standard eigenvalue problem with relatively small spectral width, an attribute that is critical to the eigensolver performance, particularly due to the absence of effective real-space preconditioners. In addition, high-order approximations can be easily incorporated, a feature that is essential for efficient electronic structure calculations. However, the lack of an underlying variational structure due to the absence of a basis can result in non-monotonic convergence of the energies and atomic forces. In addition, the reduced accuracy of spatial integrations due to the use of a lower order integration scheme can lead to a pronounced ‘egg-box’ effect [41, 42]—phenomenon arising due to the breaking of the translational symmetry—which can significantly impact the accuracy of structural relaxations and molecular dynamics simulations.

In this work, we present the second component of SPARC (Simulation Package for Ab-initio Real-space Calculations) [43]: an accurate and efficient finite-difference formulation and parallel implementation of DFT for periodic systems. The solution methodology includes a local formulation of the electrostatics, the Chebyshev polynomial filtered self-consistent field iteration, and a reformulation of the non-local force component. Through selected examples, we demonstrate that SPARC obtains high rates of convergence in the energy and forces to reference plane-wave results on refining the discretization; forces that are consistent with the energy, both being free from any noticeable ‘egg-box’ effect; and accurate ground-state properties. Moreover, we show that SPARC displays weak and strong scaling behavior that is similar to well-established plane-wave codes, but with a significantly smaller prefactor.

The remainder of this paper is organized as follows. In Section 2, we provide the mathematical details for periodic DFT. In Section 3, we describe its finite-difference formulation and parallel implementation in SPARC, whose accuracy and efficiency is verified through selected examples in Section 4. Finally, we provide concluding remarks in Section 5.

## 2. Density Functional Theory (DFT)

Consider a unit cell  $\Omega$  with  $N$  atoms and a total of  $N_e$  valence electrons. Let the nuclei be positioned at  $\mathbf{R} = \{\mathbf{R}_1, \mathbf{R}_2, \dots, \mathbf{R}_N\}$  and possess valence charges  $\{Z_1, Z_2, \dots, Z_N\}$ , respectively. Neglecting spin, the system’s free energy in Density Functional Theory (DFT) [1, 2] can be written as

$$\mathcal{F}(\Psi, \mathbf{g}, \mathbf{R}) = T_s(\Psi, \mathbf{g}) + E_{xc}(\rho) + K(\Psi, \mathbf{g}, \mathbf{R}) + E_{el}(\rho, \mathbf{R}) - TS(\mathbf{g}), \quad (1)$$

where  $\Psi = \{\psi_1, \psi_2, \dots, \psi_{N_s}\}$  is the collection of orbitals with occupations  $\mathbf{g} = \{g_1, g_2, \dots, g_{N_s}\}$ ,  $\rho$  is the electron density, and  $T$  is the electronic temperature. The electron density itself can be expressed in terms of the orbitals and their occupations as

$$\rho(\mathbf{x}) = 2 \sum_{n=1}^{N_s} \mathcal{f}_{BZ} g_n(\mathbf{k}) |\psi_n(\mathbf{x}, \mathbf{k})|^2 d\mathbf{k}, \quad (2)$$

where  $\mathbf{k}$  denotes the Bloch wavevector, and  $\mathcal{f}_{BZ}$  signifies the volume average over the Brillouin zone. In Eqn. 1, the first term is the electronic kinetic energy, the second term is the exchange-correlation energy, the third term is the non-local pseudopotential energy, the fourth term is the total electrostatic energy, and the final term is the entropic contribution arising from the partial occupations of the orbitals.

*Electronic kinetic energy.* In Kohn-Sham DFT, the kinetic energy of the non-interacting electrons takes the form

$$T_s(\Psi, \mathbf{g}) = - \sum_{n=1}^{N_s} \int_{BZ} \int_{\Omega} g_n(\mathbf{k}) \psi_n^*(\mathbf{x}, \mathbf{k}) \nabla^2 \psi_n(\mathbf{x}, \mathbf{k}) d\mathbf{x} d\mathbf{k}. \quad (3)$$

where the superscript  $*$  denotes the complex conjugate.

*Exchange-correlation energy.* The exact form of the exchange-correlation energy is currently unknown. Therefore, a number of approximations have been developed, including the widely used Local Density Approximation (LDA) [2]:

$$E_{xc}(\rho) = \int_{\Omega} \varepsilon_{xc}(\rho(\mathbf{x})) \rho(\mathbf{x}) d\mathbf{x}, \quad (4)$$

where  $\varepsilon_{xc}(\rho) = \varepsilon_x(\rho) + \varepsilon_c(\rho)$  is the sum of the exchange and correlation per particle of a uniform electron gas.

*Non-local pseudopotential energy.* The non-local pseudopotential energy within the Kleinman-Bylander [44] representation takes the form

$$K(\Psi, \mathbf{g}, \mathbf{R}) = 2 \sum_{n=1}^{N_s} \int_{BZ} g_n(\mathbf{k}) \sum_I \sum_{lm} \gamma_{Il} \left| \int_{\Omega} \chi_{Ilm}^*(\mathbf{x}, \mathbf{R}_I) \psi_n(\mathbf{x}, \mathbf{k}) d\mathbf{x} \right|^2 d\mathbf{k}, \quad (5)$$

where the coefficients  $\gamma_{Il}$  and projection functions  $\chi_{Ilm}$  can be expressed as

$$\gamma_{Il} = \left( \int_{\Omega} \chi_{Ilm}^*(\mathbf{x}, \mathbf{R}_I) u_{Ilm}(\mathbf{x}, \mathbf{R}_I) d\mathbf{x} \right)^{-1}, \quad \chi_{Ilm}(\mathbf{x}, \mathbf{R}_I) = u_{Ilm}(\mathbf{x}, \mathbf{R}_I) (V_{Il}(\mathbf{x}, \mathbf{R}_I) - V_I(\mathbf{x}, \mathbf{R}_I)). \quad (6)$$

Above,  $u_{Ilm}$  are the isolated atom pseudowavefunctions,  $V_{Il}$  are the angular momentum dependent pseudopotentials, and  $V_I$  are the local components of the pseudopotentials, with  $l$  and  $m$  signifying the azimuthal and magnetic quantum numbers, respectively. The summation index  $I$  runs over all atoms in  $\mathbb{R}^3$ , i.e., all the atoms in  $\Omega$  and their periodic images.

*Electrostatic energy.* The total electrostatic energy is the sum of three components:

$$E_{el}(\rho, \mathbf{R}) = \frac{1}{2} \int_{\mathbb{R}^3} \int_{\Omega} \frac{\rho(\mathbf{x}) \rho(\mathbf{x}')}{|\mathbf{x} - \mathbf{x}'|} d\mathbf{x} d\mathbf{x}' + \sum_I \int_{\Omega} \rho(\mathbf{x}) V_I(\mathbf{x}, \mathbf{R}_I) d\mathbf{x} + \frac{1}{2} \sum_I \sum_{\substack{J=1 \\ J \neq I}}^N \frac{Z_I Z_J}{|\mathbf{R}_I - \mathbf{R}_J|}, \quad (7)$$

where the first term—referred to as the Hartree energy—is the classical interaction energy of the electron density, the second term is the interaction energy between the electron density and the nuclei, and the third term is the repulsion energy between the nuclei. Again, the summation index  $I$  runs over all atoms in  $\mathbb{R}^3$ .

*Electronic entropy.* The electronic entropy originating from the partial orbital occupations:

$$S(\mathbf{g}) = -2k_B \sum_{n=1}^{N_s} \int_{BZ} (g_n(\mathbf{k}) \log g_n(\mathbf{k}) + (1 - g_n(\mathbf{k})) \log(1 - g_n(\mathbf{k}))) d\mathbf{k}, \quad (8)$$

where  $k_B$  is the Boltzmann constant.

*Ground state.* The overall ground state in DFT is governed by the variational problem

$$\mathcal{F}_0 = \inf_{\mathbf{R}} \hat{\mathcal{F}}(\mathbf{R}), \quad (9)$$

where

$$\hat{\mathcal{F}}(\mathbf{R}) = \inf_{\Psi, \mathbf{g}} \mathcal{F}(\Psi, \mathbf{g}, \mathbf{R}) \quad s.t. \quad \int_{\Omega} \psi_i^*(\mathbf{x}, \mathbf{k}) \psi_j(\mathbf{x}, \mathbf{k}) d\mathbf{x} = \delta_{ij}, \quad 2 \sum_{n=1}^{N_s} \int_{BZ} g_n(\mathbf{k}) d\mathbf{k} = N_e. \quad (10)$$

In this staggered approach, the electronic ground-state as described by the above equation needs to be computed for every configuration of the nuclei encountered during the geometry optimization represented by Eqn. 9.

### 3. Formulation and implementation

In this section, we describe the real-space formulation and parallel finite-difference implementation of Density Functional Theory (DFT) for periodic systems. This represents the second component of SPARC (Simulation Package for Ab-initio Real-space Calculations), a first principles code currently under development for large-scale electronic structure calculations.

*Electrostatic reformulation.* The non-locality of the electrostatic energy in Eqn. 7 makes its direct real-space evaluation scale as  $\mathcal{O}(N^2)$  with respect to the number of atoms. Furthermore, the individual components diverge in periodic systems. To overcome this, we adopt a local formulation of the electrostatics [45, 46]:

$$E_{el}(\rho, \mathbf{R}) = \sup_{\phi} \left\{ -\frac{1}{8\pi} \int_{\Omega} |\nabla \phi(\mathbf{x}, \mathbf{R})|^2 d\mathbf{x} + \int_{\Omega} (\rho(\mathbf{x}) + b(\mathbf{x}, \mathbf{R})) \phi(\mathbf{x}, \mathbf{R}) d\mathbf{x} \right\} - E_{self}(\mathbf{R}) + E_c(\mathbf{R}), \quad (11)$$

where  $\phi$  denotes the electrostatic potential. In addition,  $b$  represents the total pseudocharge density of the nuclei:

$$b(\mathbf{x}, \mathbf{R}) = \sum_I b_I(\mathbf{x}, \mathbf{R}_I), \quad b_I(\mathbf{x}, \mathbf{R}_I) = -\frac{1}{4\pi} \nabla^2 V_I(\mathbf{x}, \mathbf{R}_I), \quad (12)$$

$$\int_{\Omega} b(\mathbf{x}, \mathbf{R}) d\mathbf{x} = -N_e, \quad \int_{\mathbb{R}^3} b_I(\mathbf{x}, \mathbf{R}_I) d\mathbf{x} = Z_I, \quad (13)$$

where the summation index  $I$  runs over all atoms in  $\mathbb{R}^3$ , and  $b_I$  is the pseudocharge density of the  $I^{th}$  nucleus that generates the potential  $V_I$ . The second to last term in Eqn. 11 represents the self energy associated with the pseudocharge densities:

$$E_{self}(\mathbf{R}) = \frac{1}{2} \sum_I \int_{\Omega} b_I(\mathbf{x}, \mathbf{R}_I) V_I(\mathbf{x}, \mathbf{R}_I) d\mathbf{x}. \quad (14)$$

The last term  $E_c$ , whose explicit expression can be found in Appendix A, corrects for the error in the repulsive energy when the pseudocharge densities overlap.

*Electronic ground-state.* The electronic ground-state for a given position of nuclei is governed by the constrained minimization problem in Eqn. 10. On taking the first variation and utilizing Bloch's theorem [47]:

$$\psi_n(\mathbf{x}, \mathbf{k}) = e^{i\mathbf{k}\cdot\mathbf{x}} u_n(\mathbf{x}, \mathbf{k}), \quad (15)$$

we arrive at

$$\begin{aligned} \left( \mathcal{H} \equiv -\frac{1}{2} \nabla^2 - i\mathbf{k}\cdot\nabla + \frac{1}{2}|\mathbf{k}|^2 + V_{xc} + \phi + e^{-i\mathbf{k}\cdot\mathbf{x}} V_{nl} e^{i\mathbf{k}\cdot\mathbf{x}} \right) u_n &= \lambda_n u_n, \quad n = 1, 2, \dots, N_s, \\ g_n(\mathbf{k}) &= \left( 1 + \exp \left( \frac{\lambda_n(\mathbf{k}) - \lambda_f}{k_B T} \right) \right)^{-1}, \quad \text{where } \lambda_f \text{ is s.t. } 2 \sum_{n=1}^{N_s} \int_{BZ} g_n(\mathbf{k}) d\mathbf{k} = N_e, \\ \rho(\mathbf{x}) &= 2 \sum_{n=1}^{N_s} \int_{BZ} g_n(\mathbf{k}) |u_n(\mathbf{x}, \mathbf{k})|^2 d\mathbf{k}, \quad -\frac{1}{4\pi} \nabla^2 \phi(\mathbf{x}, \mathbf{R}) = \rho(\mathbf{x}) + b(\mathbf{x}, \mathbf{R}), \end{aligned} \quad (16)$$

where  $i = \sqrt{-1}$ ,  $u$  is a function that is periodic on the unit cell,  $\mathcal{H}$  is the Hamiltonian operator,  $V_{xc} = \delta E_{xc}/\delta\rho$  is the exchange-correlation potential,  $\lambda_f$  is the Fermi energy, and  $V_{nl}$  is the non-local pseudopotential operator:

$$V_{nl} f = \sum_I V_{nl,I} f = \sum_I \sum_{lm} \gamma_{Il} \chi_{Ilm}^* \int_{\Omega} \chi_{Ilm}^*(\mathbf{x}, \mathbf{R}_I) f(\mathbf{x}) d\mathbf{x}. \quad (17)$$

The electronic ground-state is determined by solving the non-linear eigenvalue problem in Eqn. 16 using the Self-Consistent Field (SCF) method [48]. Specifically, a fixed-point iteration is performed with respect to the potential  $V_{eff} = V_{xc} + \phi$ , which is further accelerated using mixing/extrapolation schemes [49, 50, 51, 52]. In each iteration of the SCF method, the electrostatic potential is calculated by solving the Poisson equation, and the electron density is determined by computing the eigenfunctions of the linearized Hamiltonian. The orthogonality requirement amongst the Kohn-Sham orbitals makes such a procedure scale asymptotically as  $\mathcal{O}(N^3)$  with respect to the number of atoms, which severely limits the size of systems that can be studied. To overcome this restrictive scaling,  $\mathcal{O}(N)$  approaches [21, 22] will be subsequently developed and implemented into SPARC.

*Free energy.* The free energy is evaluated using the Harris-Foulkes [53, 54] type functional:

$$\begin{aligned} \hat{\mathcal{F}}(\mathbf{R}) &= 2 \sum_{n=1}^{N_s} \int_{BZ} g_n(\mathbf{k}) \lambda_n(\mathbf{k}) d\mathbf{k} + \int_{\Omega} \varepsilon_{xc}(\rho(\mathbf{x})) \rho(\mathbf{x}) d\mathbf{x} - \int_{\Omega} V_{xc}(\rho(\mathbf{x})) \rho(\mathbf{x}) d\mathbf{x} \\ &+ \frac{1}{2} \int_{\Omega} (b(\mathbf{x}, \mathbf{R}) - \rho(\mathbf{x})) \phi(\mathbf{x}, \mathbf{R}) d\mathbf{x} - E_{self}(\mathbf{R}) + E_c(\mathbf{R}) \\ &+ 2k_B T \sum_{n=1}^{N_s} \int_{BZ} (g_n(\mathbf{k}) \log g_n(\mathbf{k}) + (1 - g_n(\mathbf{k})) \log(1 - g_n(\mathbf{k}))) d\mathbf{k}, \end{aligned} \quad (18)$$

where  $E_{self}$  and  $E_c$  are as defined in Eqns. 14 and 44, respectively.

*Atomic forces.* Once the electronic ground-state has been determined, the atomic forces are calculated using the relation:

$$\begin{aligned}
\mathbf{f}_J &= -\frac{\partial \hat{\mathcal{F}}(\mathbf{R})}{\partial \mathbf{R}_J} \\
&= \sum_{J'} \int_{\Omega} \nabla b_{J'}(\mathbf{x}, \mathbf{R}_{J'}) (\phi(\mathbf{x}, \mathbf{R}) - V_{J'}(\mathbf{x}, \mathbf{R}_{J'})) \, d\mathbf{x} + \mathbf{f}_{J,c}(\mathbf{R}) \\
&\quad - 4 \sum_{n=1}^{N_s} \int_{BZ} g_n(\mathbf{k}) \sum_{lm} \gamma_{Jl} \sum_{J'} \Re \left[ \left( \int_{\Omega} u_n^*(\mathbf{x}, \mathbf{k}) e^{-i\mathbf{k}\cdot\mathbf{x}} \chi_{J'lm}(\mathbf{x}, \mathbf{R}_{J'}) \, d\mathbf{x} \right) \left( \int_{\Omega} \nabla u_n(\mathbf{x}, \mathbf{k}) e^{i\mathbf{k}\cdot\mathbf{x}} \chi_{J'lm}^*(\mathbf{x}, \mathbf{R}_{J'}) \, d\mathbf{x} \right) \right]
\end{aligned}$$

where the summation index  $J'$  runs over the  $J^{th}$  atom and its periodic images, and  $\Re[\cdot]$  denotes the real part of the bracketed expression. The first term is the local component of the force [18], the second term corrects for overlapping pseudocharge densities [55] (Appendix A), and the final term is the non-local component obtained by transferring the derivative on the projectors (with respect to the atomic position) to the orbitals (with respect to space) [56]. This strategy is employed since the orbitals are generally much smoother than the projectors, and therefore more accurate forces can be obtained for a given discretization [57].

*Overview of SPARC.* SPARC has been implemented in the framework of the Portable, Extensible Toolkit for scientific computations (PETSc) [58, 59] suite of data structures and routines. The approach adopted for determining the ground-state is outlined in Fig. 1, whose key components are discussed in detail in the subsections below.

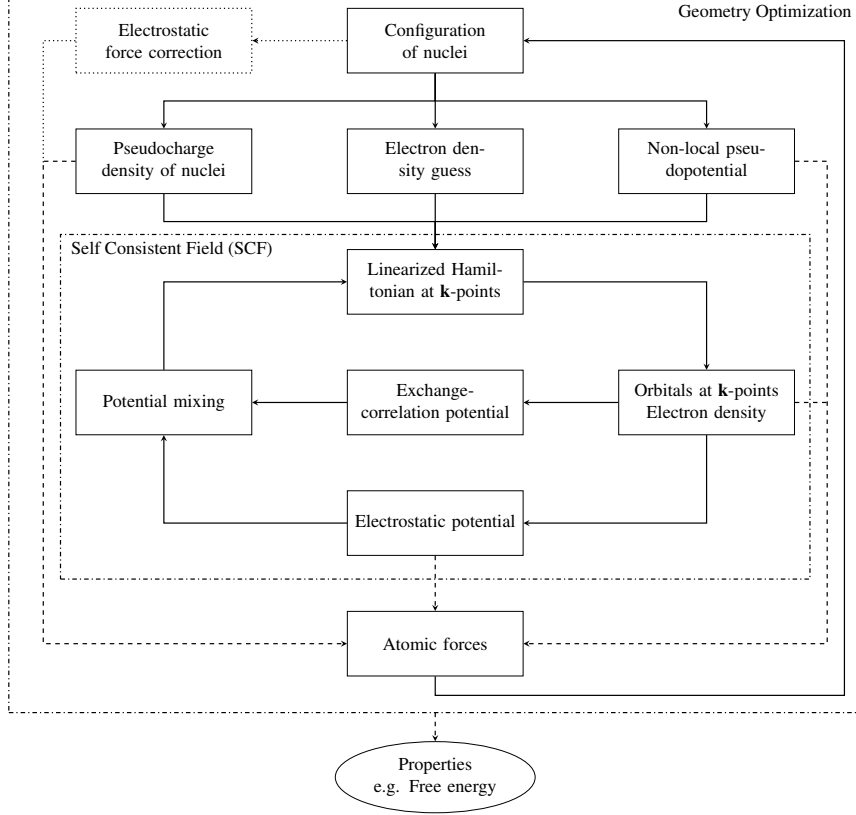


Figure 1: Outline of ground-state DFT simulations in SPARC for periodic systems.

### 3.1. Finite-difference discretization

We discretize the unit cell  $\Omega$ —cuboidal in shape with sides of length  $L_1$ ,  $L_2$  and  $L_3$ —using a uniform finite-difference grid with spacing  $h$  such that  $L_1 = n_1 h$ ,  $L_2 = n_2 h$  and  $L_3 = n_3 h$  ( $n_1, n_2, n_3 \in \mathbb{N}$ ,  $\mathbb{N}$  : set of all natural numbers). We designate each finite-difference node using an index of the form  $(i, j, k)$ , where  $i = 1, 2, \dots, n_1$ ,  $j = 1, 2, \dots, n_2$  and  $k = 1, 2, \dots, n_3$ . We approximate the Laplacian using the central finite-difference approximation:

$$\nabla_h^2 f|^{(i,j,k)} \approx \sum_{p=0}^{n_o} w_p \left( f^{(i+p,j,k)} + f^{(i-p,j,k)} + f^{(i,j+p,k)} + f^{(i,j-p,k)} + f^{(i,j,k+p)} + f^{(i,j,k-p)} \right), \quad (20)$$

where  $f^{(i,j,k)}$  represents the value of the function  $f$  at  $(i, j, k)$ , and the weights [60, 46]

$$\begin{aligned} w_0 &= -\frac{1}{h^2} \sum_{q=1}^{n_o} \frac{1}{q^2}, \\ w_p &= \frac{2(-1)^{p+1}}{h^2 p^2} \frac{(n_o!)^2}{(n_o - p)!(n_o + p)!}, \quad p = 1, 2, \dots, n_o. \end{aligned} \quad (21)$$

Similarly, we approximate the gradient operator using central finite-differences:

$$\nabla_h f|^{(i,j,k)} \approx \sum_{p=1}^{n_o} \tilde{w}_p \left( (f^{(i+p,j,k)} - f^{(i-p,j,k)}) \hat{\mathbf{e}}_1 + (f^{(i,j+p,k)} - f^{(i,j-p,k)}) \hat{\mathbf{e}}_2 + (f^{(i,j,k+p)} - f^{(i,j,k-p)}) \hat{\mathbf{e}}_3 \right), \quad (22)$$

where  $\hat{\mathbf{e}}_1, \hat{\mathbf{e}}_2$  and  $\hat{\mathbf{e}}_3$  represent unit vectors along the edges of  $\Omega$ , and the weights [60, 46]

$$\tilde{w}_p = \frac{(-1)^{p+1}}{hp} \frac{(n_o!)^2}{(n_o - p)!(n_o + p)!}, \quad p = 1, 2, \dots, n_o. \quad (23)$$

We employ the trapezoidal rule for performing spatial integrations, i.e.,

$$\int_{\Omega} f(\mathbf{x}) d\mathbf{x} \approx h^3 \sum_{i=1}^{n_1} \sum_{j=1}^{n_2} \sum_{k=1}^{n_3} f^{(i,j,k)}, \quad (24)$$

using which we approximate the nonlocal pseudopotential operator as

$$V_{nl} f^{(i,j,k)} = \sum_I V_{nl,I} f^{(i,j,k)} \approx h^3 \sum_I \sum_{lm} \sum_{p=1}^{n_1} \sum_{q=1}^{n_2} \sum_{r=1}^{n_3} \gamma_{II} \chi_{Ilm}^{(i,j,k)} \chi_{Ilm}^{*(p,q,r)} f^{(p,q,r)}, \quad (25)$$

where the summation index  $I$  runs over all the atoms in  $\mathbb{R}^3$ . We enforce periodic boundary conditions on  $\Omega$  by mapping any index that does not correspond to a node in the finite-difference grid to its periodic image within  $\Omega$ .

Henceforth, we denote the discrete Hamiltonian matrix as a function of the Bloch wavevector  $\mathbf{k}$  by  $\mathbf{H}(\mathbf{k}) \in \mathbb{C}^{N_d \times N_d}$ , where  $N_d = n_1 \times n_2 \times n_3$  is the total number of finite-difference nodes. In addition, we represent the eigenvalues of  $\mathbf{H}(\mathbf{k})$  arranged in ascending order by  $\lambda_1(\mathbf{k}), \lambda_2(\mathbf{k}), \dots, \lambda_{N_d}(\mathbf{k})$ . We store  $\mathbf{H}(\mathbf{k})$  and other sparse matrices in compressed row format, and store the discrete cell periodic part of the orbitals as columns of the dense matrix  $\mathbf{U}(\mathbf{k}) \in \mathbb{C}^{N_d \times N_s}$ . In parallel computations, we partition the domain as  $\Omega = \bigcup_{p=1}^{n_p} \Omega_p$ , where  $\Omega_p$  denotes the domain local to the  $p^{th}$  processor, and  $n_p$  is the total number of processors. The specific choice of  $\Omega_p$  corresponds to the PETSc default for structured grids.

### 3.2. Pseudocharge density generation and self energy calculation

In each structural relaxation step, the finite-difference Laplacian is used to assign the pseudocharge densities to the grid [18]:

$$b^{(i,j,k)} = \sum_I b_I^{(i,j,k)}, \quad b_I^{(i,j,k)} = -\frac{1}{4\pi} \nabla_h^2 V_I^{(i,j,k)}, \quad (26)$$

where the summation index  $I$  runs over all atoms in  $\mathbb{R}^3$ . The discrete form of the pseudocharge density  $b_I$  has exponential decay away from  $\mathbf{R}_I$ , as demonstrated in Appendix B. This allows for its truncation at some suitably chosen radius  $r_I^b$ , without appreciable loss of accuracy. The corresponding discrete self energy takes the form

$$E_{self}^h = \frac{1}{2} h^3 \sum_I \sum_{i=1}^{n_1} \sum_{j=1}^{n_2} \sum_{k=1}^{n_3} b_I^{(i,j,k)} V_I^{(i,j,k)}. \quad (27)$$

In Algorithm 1, we outline the calculation of  $b^{(i,j,k)}$  and  $E_{self}^h$ , as implemented in SPARC. For the  $J^{th}$  atom in  $\Omega$ , we determine  $\Omega_{r_{J'}^b} \cap \Omega_p$  (with  $s$  and  $e$  denoting the starting and ending indices) for atoms which have  $\Omega_{r_{J'}^b} \cap \Omega \neq \emptyset$ . Here, the index  $J'$  signifies the  $J^{th}$  atom and its periodic images. Further,  $\Omega_{r_{J'}^b}$  denotes the cube with side of length  $2r_J^b$  centered on the  $J^{th}$  atom and  $\Omega_p$  represents the domain local to the  $p^{th}$  processor. We have chosen  $\Omega_{r_{J'}^b}$  to be a cube rather than a sphere due to its simplicity and efficiency within

the Euclidean finite-difference discretization. The values of  $r_J^b$  are chosen such that the charge constraint in Eqn. 13 is satisfied to within a prespecified tolerance  $\varepsilon_b$ , i.e.,

$$\left| h^3 \sum_{J'} \sum_{i=1}^{n_1} \sum_{j=1}^{n_2} \sum_{k=1}^{n_3} b_{J'}^{(i,j,k)} - Z_J \right| < \varepsilon_b, \quad (28)$$

where the summation index  $J'$  runs over the  $J^{th}$  atom and its periodic images. In the overlap region so established, we interpolate the values of  $V_{J'}^{(i,j,k)}$  on to the finite-difference grid using cubic-splines [61]. Next, we determine  $b^{(i,j,k)}$  and  $E_{self}^{h,p}$ —contribution of the  $p^{th}$  processor to the self energy—using Eqns. 26 and 27, respectively. Finally, we calculate the total self energy  $E_{self}^h$  by summing the contributions from all the processors.

---

**Algorithm 1:** Pseudocharge density generation and self energy calculation

---

**Input:**  $\mathbf{R}$ ,  $V_J$ , and  $r_J^b$   
 $b^{(i,j,k)} = 0$ ,  $E_{self}^{h,p} = 0$   
**for**  $J = 1 \dots N$  **do**  
  **for**  $J' = J^{th}$  atom and its periodic images for which  $\Omega_{r_{J'}^b} \cap \Omega \neq \emptyset$  **do**  
    Determine  $i_s, i_e, j_s, j_e, k_s, k_e$  of  $\Omega_{r_{J'}^b} \cap \Omega_p$   
    Determine  $V_{J'}^{(i,j,k)} \forall i \in [i_s - n_o, i_e + n_o], j \in [j_s - n_o, j_e + n_o], k \in [k_s - n_o, k_e + n_o]$   
     $b_{J'}^{(i,j,k)} = -\frac{1}{4\pi} \nabla_h^2 V_{J'}^{(i,j,k)}$ ,  $b^{(i,j,k)} = b^{(i,j,k)} + b_{J'}^{(i,j,k)} \forall i \in [i_s, i_e], j \in [j_s, j_e], k \in [k_s, k_e]$   
     $E_{self}^{h,p} = E_{self}^{h,p} + \frac{1}{2} h^3 b_{J'}^{(i,j,k)} V_{J'}^{(i,j,k)} \forall i \in [i_s, i_e], j \in [j_s, j_e], k \in [k_s, k_e]$   
   $E_{self}^h = \sum_{p=1}^{n_p} E_{self}^{h,p}$   
**Output:**  $b^{(i,j,k)}$  and  $E_{self}^h$

---

### 3.3. Brillouin zone integration

The volume averaged integral of any function over the Brillouin zone is approximated as

$$\oint_{BZ} f(\mathbf{k}) d\mathbf{k} \approx \sum_{b=1}^{N_k} w_b f_b, \quad (29)$$

where  $f_b \equiv f(\mathbf{k}_b)$ . Here,  $\mathbf{k}_b$  and  $w_b$  ( $b = 1, 2, \dots, N_k$ ) denote the nodes and weights for integration, respectively. The specific choice of  $\mathbf{k}_b$  is commonly referred to as Brillouin zone sampling.

### 3.4. Electron density calculation

On employing the Brillouin zone integration scheme described by Eqn. 29, the electron density takes the form

$$\rho(\mathbf{x}) = 2 \sum_{n=1}^{N_s} \sum_{b=1}^{N_k} w_b g_{nb} |u_{nb}(\mathbf{x})|^2. \quad (30)$$

In each SCF iteration, we calculate the electron density using the Chebyshev-filtered subspace iteration (CheFSI) method [62, 63], wherein we compute approximations to the eigenvectors corresponding to the lowest  $N_s$  eigenvalues of  $\mathbf{H}_b$ ,  $b = 1, 2, \dots, N_k$ . This choice of eigensolver is motivated by the minimal

orthogonalization and computer memory costs compared to other alternatives commonly employed in electronic structure calculations, e.g. Locally Optimal Block Preconditioned Conjugate Gradient (LOBPCG) [64].

The implementation of the CheFSI algorithm in SPARC consists of three main components. First, we use the rapid growth of Chebyshev polynomials outside the interval  $[-1, 1]$  to filter out the unwanted eigencomponents from  $\mathbf{U}_b$ :

$$\mathbf{U}_{bf} = p_{mb}(\mathbf{H}_b)\mathbf{U}_b, \quad p_{mb}(t) = C_m \left( \frac{t - c_b}{e_b} \right), \quad b = 1, 2, \dots, N_k, \quad (31)$$

where the columns of  $\mathbf{U}_{bf}$  represent the filtered cell periodic part of the orbitals, and  $C_m$  denotes the Chebyshev polynomial of degree  $m$ . Additionally,  $e_b = (\lambda_{N_d b} - \lambda_c)/2$  and  $c_b = (\lambda_{N_d b} + \lambda_c)/2$ , where  $\lambda_c$  is the filter cutoff. Rather than explicitly compute the matrix  $p_{mb}(\mathbf{H}_b)$ , its product with  $\mathbf{U}_b$  is determined using the three term recurrence relation for Chebyshev polynomials.

Next, projecting onto the filtered basis  $\mathbf{U}_{bf}$ , we arrive at the generalized eigenproblem:

$$\tilde{\mathbf{H}}_b \mathbf{y}_{nb} = \lambda_{nb} \tilde{\mathbf{M}}_b \mathbf{y}_{nb}, \quad n = 1, 2, \dots, N_s, \quad b = 1, 2, \dots, N_k, \quad (32)$$

where  $\lambda_{nb}$  represent approximations to the eigenvalues of  $\mathbf{H}_b$ , and the dense matrices  $\tilde{\mathbf{H}}_b, \tilde{\mathbf{M}}_b \in \mathbb{C}^{N_s \times N_s}$  are determined as

$$\tilde{\mathbf{H}}_b = \mathbf{U}_{bf}^* \mathbf{H}_b \mathbf{U}_{bf}, \quad \tilde{\mathbf{M}}_b = \mathbf{U}_{bf}^* \mathbf{M}_b \mathbf{U}_{bf}. \quad (33)$$

After eigendecomposing Eqn. 32 at all the  $\mathbf{k}$ -points, the Fermi energy  $\lambda_f$  is calculated by enforcing the constraint on the total number of electrons:

$$2 \sum_{n=1}^{N_s} \sum_{b=1}^{N_k} w_b g_{nb} = N_e, \quad \text{where} \quad g_{nb} = \left( 1 + \exp \left( \frac{\lambda_{nb} - \lambda_f}{k_B T} \right) \right)^{-1}. \quad (34)$$

Finally, we perform the subspace rotation

$$\mathbf{U}_b = \mathbf{U}_{bf} \mathbf{Y}_b, \quad b = 1, 2, \dots, N_k, \quad (35)$$

where the columns of the matrix  $\mathbf{Y}_b \in \mathbb{C}^{N_s \times N_s}$  contain the eigenvectors  $\mathbf{y}_{nb}$ . The columns of  $\mathbf{U}_b$  so obtained represent approximations to the eigenvectors of  $\mathbf{H}_b$ . The electron density at the finite-difference grid points is then calculated using the relation

$$\rho^{(i,j,k)} = 2 \sum_{n=1}^{N_s} \sum_{b=1}^{N_k} w_b g_{nb} |u_{nb}^{(i,j,k)}|^2, \quad (36)$$

where the values of  $u_{nb}^{(i,j,k)}$  are extracted from the  $n^{th}$  column of  $\mathbf{U}_b$ .

We start the very first SCF iteration of the complete DFT simulation with a randomly generated guess for  $\mathbf{U}_b$  ( $b = 1, 2, \dots, N_k$ ), and perform the CheFSI steps multiple times [65] without calculating/updating the electron density. This allows us to obtain a good approximation of the electron density for the second SCF iteration. For every subsequent SCF iteration, we perform the CheFSI steps only once, and use the rotated  $\mathbf{U}_b$  from the previous step as the initial guess. Overall, the calculation of the electron density scales as  $\mathcal{O}(N_k N_s N_d) + \mathcal{O}(N_k N_s^2 N_d) + \mathcal{O}(N_k N_s^3)$ , which makes it  $\mathcal{O}(N^3)$  with respect to the number of atoms.

### 3.5. Free energy calculation

On approximating the spatial and Brillouin zone integrals using Eqns. 24 and 29, respectively, we arrive at the discrete form for the free energy at the electronic ground-state:

$$\begin{aligned} \hat{\mathcal{F}}^h &= 2 \sum_{n=1}^{N_s} \sum_{b=1}^{N_k} w_b g_{nb} \lambda_{nb} + h^3 \sum_{i=1}^{n_1} \sum_{j=1}^{n_2} \sum_{k=1}^{n_3} \left( \varepsilon_{xc}^{(i,j,k)} \rho^{(i,j,k)} - V_{xc}^{(i,j,k)} \rho^{(i,j,k)} + \frac{1}{2} (b^{(i,j,k)} - \rho^{(i,j,k)}) \phi^{(i,j,k)} \right) \\ &\quad - E_{self}^h + E_c^h + 2k_B T \sum_{n=1}^{N_s} \sum_{b=1}^{N_k} w_b (g_{nb} \log g_{nb} + (1 - g_{nb}) \log(1 - g_{nb})) , \end{aligned} \quad (37)$$

where  $E_{self}^h$  is the discrete self energy (Eqn. 27), and  $E_c^h$  is the discrete repulsive energy correction for overlapping pseudocharges (Eqn. 48). The evaluation of  $\hat{\mathcal{F}}^h$  scales as  $\mathcal{O}(N_d)$ , and therefore  $\mathcal{O}(N)$  with respect to the number of atoms.

### 3.6. Atomic forces calculation

The discrete form of the atomic force presented in Eqn. 19 can be split into three parts:

$$\mathbf{f}_J^h = \mathbf{f}_{J,loc}^h + \mathbf{f}_{J,c}^h + \mathbf{f}_{J,nloc}^h , \quad (38)$$

where  $\mathbf{f}_{J,loc}^h$  is the discrete local component,  $\mathbf{f}_{J,c}^h$  is the discrete correction corresponding to overlapping pseudocharges, and  $\mathbf{f}_{J,nloc}^h$  is the discrete non-local component of the force. Below, we discuss the evaluation of  $\mathbf{f}_{J,loc}^h$  and  $\mathbf{f}_{J,nloc}^h$  in SPARC, with the computation of  $\mathbf{f}_{J,c}^h$  proceeding similarly to  $\mathbf{f}_{J,loc}^h$ .

*Local component.* On approximating the spatial integral using Eqn. 24, the discrete local component of the force takes the form

$$\mathbf{f}_{J,loc}^h = h^3 \sum_{J'} \sum_{i=1}^{n_1} \sum_{j=1}^{n_2} \sum_{k=1}^{n_3} \nabla_h b_{J'}^{(i,j,k)} (\phi^{(i,j,k)} - V_{J'}^{(i,j,k)}) , \quad (39)$$

where the summation index  $J'$  runs over the  $J^{th}$  atom and its periodic images. The calculation of  $\mathbf{f}_{J,loc}^h$  in SPARC is outlined in Algorithm 2, which proceeds as follows. For the  $J^{th}$  atom in  $\Omega$ , we determine  $\Omega_{r_{J'}^b} \cap \Omega_p$  (with  $s$  and  $e$  denoting the starting and ending indices) for atoms which have  $\Omega_{r_{J'}^b} \cap \Omega \neq \emptyset$ . Here, the index  $J'$  signifies the  $J^{th}$  atom and its periodic images. In this overlap region, the values of  $V_{J'}^{(i,j,k)}$  are interpolated on to the finite-difference grid using cubic-splines, from which  $b_{J'}^{(i,j,k)}$  is calculated using Eqn. 26. Subsequently,  $\mathbf{f}_{J,loc}^{h,p}$ —contribution of the  $p^{th}$  processor to the local component of the force—is calculated using Eqn. 39. Finally, the contributions from all processors are summed to simultaneously

obtain  $\mathbf{f}_{J,loc}^h$  for all the atoms.

---

**Algorithm 2:** Calculation of the local component of the atomic force.

---

**Input:**  $\mathbf{R}$ ,  $\phi^{(i,j,k)}$ ,  $V_J$ , and  $r_J^b$

**for**  $J = 1 \dots N$  **do**

$\mathbf{f}_{J,loc}^{h,p} = 0$

**for**  $J' = J^{th}$  atom and its periodic images for which  $\Omega_{r_{J'}^b} \cap \Omega \neq \emptyset$  **do**

Determine  $i_s, i_e, j_s, j_e, k_s, k_e$  of  $\Omega_{r_{J'}^b} \cap \Omega_p$

Determine  $V_{J'}^{(i,j,k)} \forall i \in [i_s - n_o, i_e + n_o], j \in [j_s - n_o, j_e + n_o]$ , and  $k \in [k_s - n_o, k_e + n_o]$

$b_{J'}^{(i,j,k)} = -\frac{1}{4\pi} \nabla_h^2 V_{J'} \Big|^{(i,j,k)} \forall i \in [i_s, i_e], j \in [j_s, j_e], k \in [k_s, k_e]$

$\mathbf{f}_{J,loc}^{h,p} = \mathbf{f}_{J,loc}^{h,p} + h^3 \sum_{i=i_s+n_o}^{i_e-n_o} \sum_{j=j_s+n_o}^{j_e-n_o} \sum_{k=k_s+n_o}^{k_e-n_o} \nabla_h b_{J'} \Big|^{(i,j,k)} (\phi^{(i,j,k)} - V_{J'}^{(i,j,k)})$

$\mathbf{f}_{J,loc}^h = \sum_{p=1}^{n_p} \mathbf{f}_{J,loc}^{h,p}$

**Output:**  $\mathbf{f}_{J,loc}^h$

---

*Non-local component.* On approximating the spatial integral using Eqn. 24, the discrete non-local component of the force takes the form

$$\mathbf{f}_{J,nloc}^h = -4 \sum_{n=1}^{N_s} \sum_{b=1}^{N_k} w_b g_{nb} \sum_{lm} \gamma_{Jl} \sum_{J'} \Re [Y_{J'nblm} \mathbf{W}_{J'nblm}] , \quad (40)$$

where

$$Y_{J'nblm} = h^3 \sum_{i=1}^{n_1} \sum_{j=1}^{n_2} \sum_{k=1}^{n_3} u_n^{*(i,j,k)} e^{-i\mathbf{k}_b \cdot \mathbf{x}^{(i,j,k)}} \chi_{J'lm}^{(i,j,k)} , \quad (41)$$

$$\mathbf{W}_{J'nblm} = h^3 \sum_{i=1}^{n_1} \sum_{j=1}^{n_2} \sum_{k=1}^{n_3} \nabla_h u_n \Big|^{(i,j,k)} e^{i\mathbf{k}_b \cdot \mathbf{x}^{(i,j,k)}} \chi_{J'lm}^{*(i,j,k)} . \quad (42)$$

The calculation of  $\mathbf{f}_{J,nloc}^h$  in SPARC is outlined in Algorithm 3, which proceeds as follows. For the  $J^{th}$  atom in  $\Omega$ , we determine  $\Omega_{r_{J'}^c} \cap \Omega_p$  (with  $s$  and  $e$  denoting the starting and ending indices) for atoms which have  $\Omega_{r_{J'}^c} \cap \Omega \neq \emptyset$ . Here, the index  $J'$  represents the  $J^{th}$  atom and its periodic images. In addition,  $\Omega_{r_{J'}^c}$  denotes the cube with side of length  $2r_J^c$  centered on the  $J^{th}$  atom. We have chosen  $\Omega_{r_{J'}^c}$  to be a cube rather than a sphere due to its simplicity and efficiency within the Euclidean finite-difference discretization. In the overlap region so determined, we interpolate the radial components of the projectors  $\chi_{J'lm}^{(i,j,k)}$  on to the finite-difference grid using cubic-splines. Next, we utilize Eqns. 41 and 42 to determine  $Y_{J'nblm}^p$  and  $\mathbf{W}_{J'nblm}^p$ , respectively, which represent the contributions of the  $p^{th}$  processor to  $Y_{J'nblm}$  and  $\mathbf{W}_{J'nblm}$ , respectively. Finally, we sum the contributions from all the processors to obtain  $Y_{J'nblm}$  and  $\mathbf{W}_{J'nblm}$ , which are then used

to calculate  $\mathbf{f}_{J,nloc}^h$  using Eqn. 40 .

---

**Algorithm 3:** Calculation of the non-local component of the atomic force

---

**Input:**  $\mathbf{R}$ ,  $\psi_n^{(i,j,k)}$ ,  $\gamma_{Jl}$ ,  $\chi_{Jlm}$ , and  $r_J^c$

**for**  $J = 1 \dots N$  **do**

**for**  $J' = J^{th}$  atom and its periodic images for which  $\Omega_{r_{J'}^c} \cap \Omega \neq \emptyset$  **do**

Determine starting and ending indices  $i_s, i_e, j_s, j_e, k_s, k_e$  for  $\Omega_{r_{J'}^c} \cap \Omega_p$

Determine  $\chi_{J'lm}^{(i,j,k)} \forall i \in [i_s, i_e], j \in [j_s, j_e], k \in [k_s, k_e]$

$Y_{J'nblm}^p = h^3 u_n^{*(i,j,k)} e^{-i\mathbf{k}_b \cdot \mathbf{x}^{(i,j,k)}} \chi_{J'lm}^{(i,j,k)} \forall i \in [i_s, i_e], j \in [j_s, j_e], k \in [k_s, k_e]$

$\mathbf{W}_{J'nblm}^p = h^3 \nabla_h u_n |^{(i,j,k)} e^{i\mathbf{k}_b \cdot \mathbf{x}^{(i,j,k)}} \chi_{J'lm}^{*(i,j,k)} \forall i \in [i_s, i_e], j \in [j_s, j_e], k \in [k_s, k_e]$

$Y_{J'nblm} = \sum_{p=1}^{n_p} Y_{J'nblm}^p$ ,  $\mathbf{W}_{J'nblm} = \sum_{p=1}^{n_p} \mathbf{W}_{J'nblm}^p$

$\mathbf{f}_{J,nloc}^h = -4 \sum_{n=1}^{N_s} \sum_{b=1}^{N_k} w_b g_{nb} \sum_{lm} \gamma_{Jl} \sum_{J'} \Re [Y_{J'nblm} \mathbf{W}_{J'nblm}]$

**Output:**  $\mathbf{f}_{J,nloc}^h$

---

## 4. Examples and Results

In this section, we verify the accuracy and efficiency of SPARC (Simulation Package for Ab-initio Real-space Calculations) for periodic Density Functional Theory (DFT) calculations. In all examples, we utilize a twelfth-order accurate finite-difference discretization, the Perdew-Wang parametrization [66] of the correlation energy calculated by Ceperley-Alder [67], norm-conserving Troullier-Martins pseudopotentials [68], and a smearing of  $k_B T = 0.01$  Ha. The cutoff radii for the non-local projectors and the local component of the pseudopotentials are listed in Appendix B. The Monkhorst-Pack [69] grid is used for performing integrations over the Brillouin zone. Unless specified otherwise, the simulations correspond to  $\mathbf{k} = [0.0 \ 0.0 \ 0.0]$  ( $\Gamma$ -point).

We solve the linear system corresponding to the Poisson problem using the block-Jacobi preconditioned [70] minimal residual method (MINRES) [71]. Within the CheFSI approach, we utilize a polynomial of degree  $m = 20$  for Chebyshev filtering; the Lanczos method [72] for calculating the extremal eigenvalues of the Hamiltonian  $\mathbf{H}_b$ ; and LAPACK's [73] implementation of the QR algorithm [74] for solving the subspace eigenproblem in Eqn. 32. We calculate the Fermi energy using Brent's method [75], and use Anderson extrapolation [76] with relaxation parameter of 0.3 and mixing history of 7 for accelerating the convergence of the SCF method. Finally, we employ the Polak-Ribiere variant of non-linear conjugate gradients with a secant line search [77] for geometry optimization.

All the results presented here are converged to within the chemical accuracy of 0.001 Ha/atom in the energy and 0.001 Ha/Bohr in the forces. Wherever applicable, the results obtained by SPARC are compared to the well-established plane-wave code ABINIT [9, 78, 79]. The error in energy is defined to be the difference in the magnitude, and the error in forces is defined to be the maximum difference in any component. All simulations are performed on a computer cluster consisting of 16 nodes with the following configuration: Altus 1804i Server - 4P Interlagos Node, Quad AMD Opteron 6276, 16C, 2.3 GHz, 128GB, DDR3-1333 ECC, 80GB SSD, MLC, 2.5" HCA, Mellanox ConnectX 2, 1-port QSFP, QDR, memfree, CentOS, Version 5, and connected through InfiniBand cable.

### 4.1. Convergence with discretization

First, we verify convergence of the energy and atomic forces computed by SPARC with respect to spatial discretization. For this study, we choose three examples:  $2 \times 2 \times 2$  unit cells of lithium hydride

with lattice constant of 7.37 Bohr and corner lithium atom perturbed by [0.57 0.43 0.37] Bohr;  $2 \times 2 \times 2$  unit cells of silicon with lattice constant of 10.68 Bohr and corner atom perturbed by [0.93 0.50 0.20] Bohr; and  $2 \times 2 \times 2$  unit cells of gold with lattice constant of 8.0 Bohr, one of the domain face-centered atoms perturbed by [0.85 0.50 0.30] Bohr, and  $1 \times 1 \times 2$  Brillouin zone integration. All errors are defined with respect to ABINIT, wherein we employ plane-wave cutoffs of 46, 40, and 46 Ha for lithium hydride, silicon, and gold, respectively, which results in energy and forces that are converged to within  $5 \times 10^{-6}$  Ha/atom and  $5 \times 10^{-6}$  Ha/Bohr, respectively.

It is clear from Fig. 2—plots of the error in energy and atomic forces with respect to mesh-size—that there is systematic convergence to the reference plane-wave result. On performing a fit to the data, we obtain average convergence rates of approximately  $\mathcal{O}(h^{10})$  in the energy and  $\mathcal{O}(h^9)$  in the forces. In doing so, the chemical accuracy desired in electronic structure calculations is readily attained. These results demonstrate that SPARC is able to obtain high convergence rates in both the energy and forces, which contributes to its accuracy and efficiency. Moreover, they converge at comparable rates, without need of additional measures such as double-grid [80] or high-order integration [42] techniques.

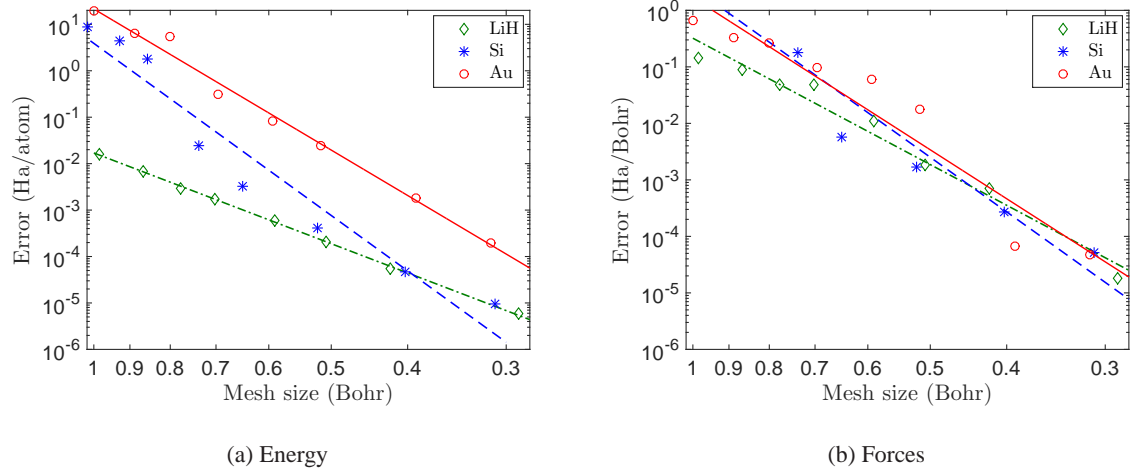


Figure 2: Convergence of the energy and atomic forces with respect to mesh size to reference planewave result for the lithium hydride, silicon, and gold systems.

#### 4.2. Bulk properties

We now verify the ability of SPARC to accurately calculate material bulk properties. We select silicon—8-atom unit cell with  $4 \times 4 \times 4$  Brillouin zone integration—as the representative example. In SPARC, we use a mesh-size of  $h = 0.407$  Bohr. We compare the results with ABINIT, wherein we choose a plane-wave energy cutoff of 40 Ha, which results in energies that are converged to within  $5 \times 10^{-6}$  Ha/atom. In Fig. 3, we plot the energy so computed by SPARC and ABINIT as a function of the lattice constant. We observe that there is very good agreement between SPARC and ABINIT, with the curves being practically indistinguishable. From a cubic fit to the data, we find that the predicted equilibrium lattice constant, energy, and bulk modulus are in agreement to within 0.003 Bohr,  $1 \times 10^{-5}$  Ha/atom, and 0.18 GPa, respectively.

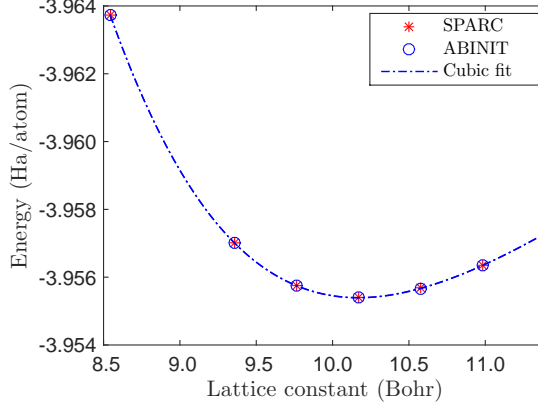


Figure 3: Variation of energy with lattice constant for silicon.

Next, we compare the band structure plot at the equilibrium lattice constants determined above, i.e., 10.157 Bohr for SPARC and 10.160 Bohr for ABINIT. Specifically, we choose the  $L - \Gamma - X - \Gamma$  circuit, whose coordinates in terms of the reciprocal lattice vectors are  $[-0.5 0.5 0.5]$ ,  $[0.0 0.0 0.0]$ ,  $[1.0 0.0 0.0]$ , and  $[1.0 1.0 1.0]$ , respectively. We discretize the  $L - \Gamma$ ,  $\Gamma - X$ , and  $X - \Gamma$  line segments into 10, 12, and 17 divisions, respectively. At each resulting  $\mathbf{k}$ -point, we determine the band structure (at the electronic ground-state) in SPARC by repeating the CheFSI steps until convergence. In Fig. 4, we present the band structure plot so computed by SPARC and compare it with that calculated by ABINIT. It is clear that there is very good agreement, with the curves being nearly identical. In particular, the HOMO eigenvalue, LUMO eigenvalue, and bandgap are in agreement to within  $7 \times 10^{-5}$  Ha,  $1 \times 10^{-5}$  Ha, and  $6 \times 10^{-5}$  Ha, respectively.

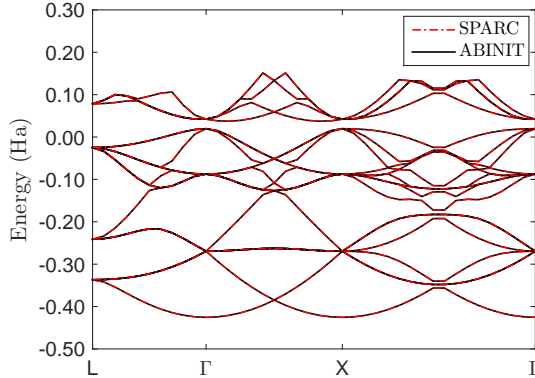


Figure 4: Band structure plot for silicon.

#### 4.3. Geometry optimization

We now verify the capacity of SPARC to perform accurate geometry optimizations. To do so, we first check the consistency of the atomic forces with the energy. As representative examples, we select single unit cells of lithium and silicon with lattice constants of 6.59 Bohr and 10.16 Bohr, respectively, and discretize them using mesh sizes of  $h = 0.287$  Bohr and 0.248 Bohr, respectively. In Fig. 5, we plot the variation in energy and force when the body centered lithium atom is displaced along the body diagonal, and one of

the face centered silicon atoms is displaced along the face diagonal. Specifically, in Fig. 5a, we plot the computed energy and its curve fit using cubic splines. In Fig. 5b, we plot the computed atomic force and the derivative of the cubic spline fit to the energy. The evident agreement demonstrates that the computed energy and atomic forces are indeed consistent. Moreover, there is no noticeable ‘egg-box’ effect [81]—a phenomenon arising due to the breaking of the translational symmetry—at meshes required for obtaining chemical accuracies.

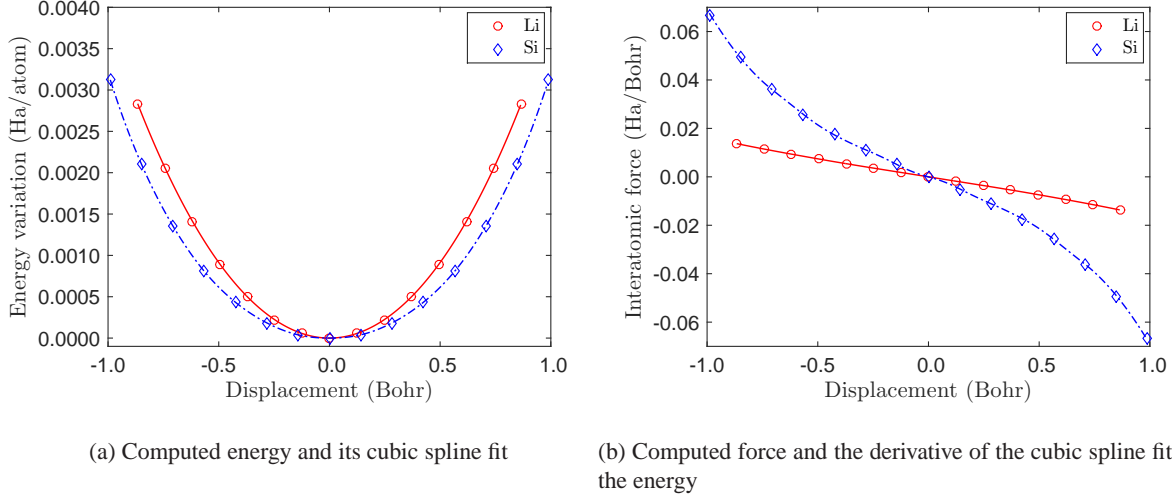


Figure 5: Variation in the energy and atomic force as a function of atomic displacement. In lithium, the body centered lithium atom is displaced along the body diagonal. In silicon, one of the face centered silicon atoms is displaced along the face diagonal.

Next, we determine the overall ground-state using SPARC for two systems:  $3 \times 3 \times 3$  unit cells of lithium and  $2 \times 2 \times 2$  unit cells of silicon, both with a vacancy. We compare the results with ABINIT, wherein we use plane wave cutoffs of 30 Ha and 40 Ha for lithium and silicon, respectively, which results in energy and forces that are converged to within  $5 \times 10^{-6}$  Ha/atom and  $5 \times 10^{-6}$  Ha/Bohr, respectively. We calculate the vacancy formation energy  $\mathcal{E}_{vf}$  using the relation [82]

$$\mathcal{E}_{vf} = \mathcal{F}_0 \left( N - 1, 1, \frac{N - 1}{N} \Omega \right) - \left( \frac{N - 1}{N} \right) \mathcal{F}_0(N, 0, \Omega), \quad (43)$$

where  $\mathcal{F}_0(N, n_v, \Omega)$  denotes the energy of the system in  $\Omega$  with  $N$  occupied lattice sites and  $n_v$  vacancies. The vacancy formation energies so computed by SPARC and ABINIT are in agreement to within  $8 \times 10^{-5}$  Ha. In addition, the fully relaxed atomic positions differ by no more than 0.01 Bohr. The contours of electron density on the mid-plane of these systems are plotted in Fig. 6. Overall we conclude that SPARC is able to accurately perform geometry optimization. Furthermore, the quality of atomic forces makes it suitable for performing ab-initio molecular dynamics [83].

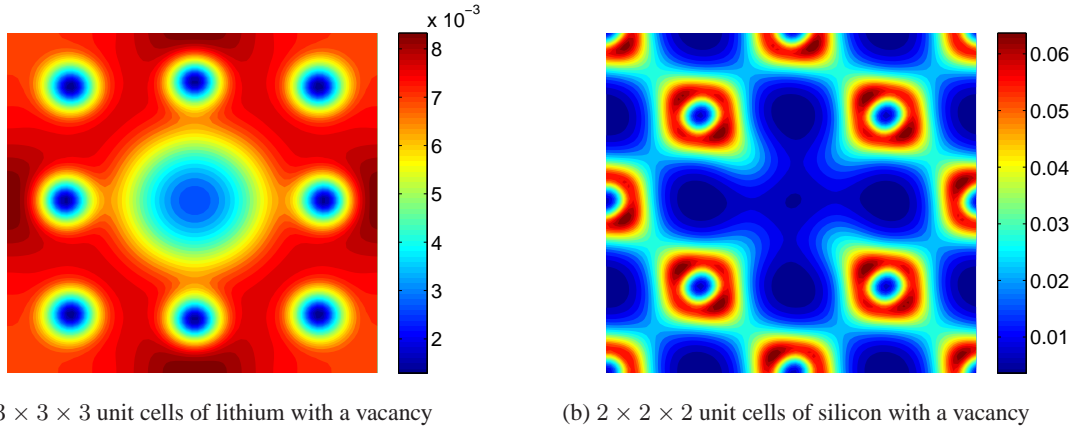


Figure 6: Mid-plane electron density contours.

#### 4.4. Scaling and Performance

Having verified the accuracy of SPARC relative to ABINIT in previous subsections, we now compare their efficiency. As representative systems, we choose  $n \times n \times n$  ( $n \in \mathbb{N}$ ) unit cells of aluminum with a vacancy. In SPARC, we employ a mesh-size of  $h = 0.778$  Bohr and Chebyshev polynomial filter of degree 15. In ABINIT, we use a plane-wave energy cutoff of 9 Ha. We choose all the other parameters in both codes so as to achieve an overall accuracy of  $5 \times 10^{-4}$  Ha/atom and  $5 \times 10^{-4}$  Ha/Bohr in the energy and forces, respectively. The times reported here include the calculation of the electronic ground-state as well as the atomic forces.

First, we compare the strong scaling of SPARC with ABINIT for  $6 \times 6 \times 6$  FCC unit cells of aluminum with a vacancy. We utilize 4, 8, 64, 144, 480, and 576 cores for performing the simulation with ABINIT, which it suggests is optimal in the range of 1 to 1000 cores. For SPARC, we select 4, 8, 27, 128, 384, and 512 cores. In Fig. 7a, we plot the wall time taken by SPARC and ABINIT as a function of the number of processors. We observe that both SPARC and ABINIT display similar trends with respect to strong scaling, with curves being close to parallel and no further reduction in wall time observed after approximately 600 cores. However, the prefactors of SPARC are up to a factor of 4 smaller than ABINIT.

Next, we compare the weak scaling of SPARC with ABINIT for  $3 \times 3 \times 3$ ,  $4 \times 4 \times 4$ ,  $5 \times 5 \times 5$ ,  $6 \times 6 \times 6$ , and  $7 \times 7 \times 7$  unit cells of aluminum, each with a vacancy. The number of electrons in these systems range from 321 to 4116. For both SPARC and ABINIT, we fix the number of electrons per core to be approximately 96, and choose at most 4 cores from every compute node. In Figure 7b, we present the results so obtained for the variation in total CPU time versus the number of electrons. We again observe similar scaling for both SPARC ( $\mathcal{O}(N_e^{3.48})$ ) and ABINIT ( $\mathcal{O}(N_e^{3.67})$ ). However, the prefactor for SPARC is again noticeably smaller, with speedups over ABINIT ranging from factors of 2.5 to 10. We note that the worse than  $\mathcal{O}(N_e^3)$  scaling of both SPARC and ABINIT is a consequence of the increase in the number of SCF iterations with system size. In fact, the average time per SCF iteration in SPARC and ABINIT scales as  $\mathcal{O}(N_e^{2.56})$  and  $\mathcal{O}(N_e^{2.8})$ , respectively.

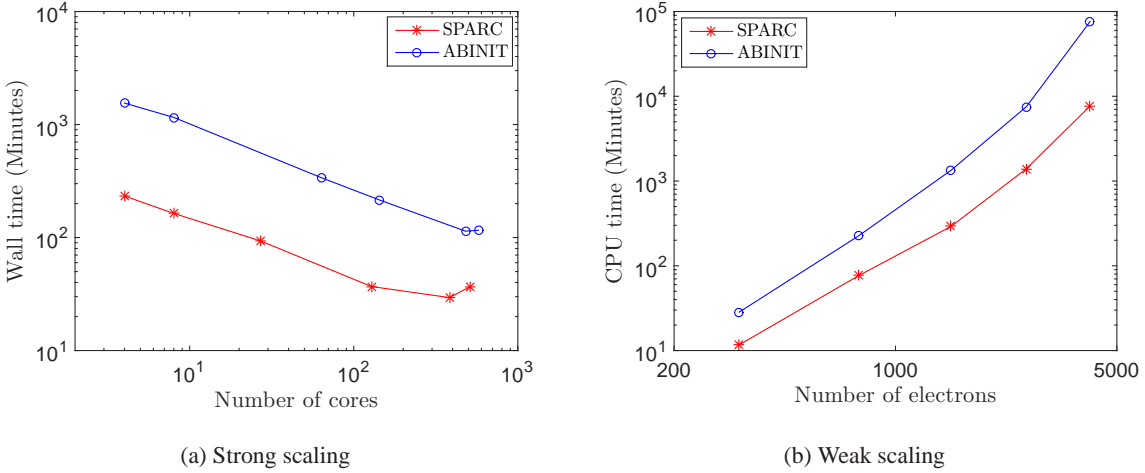


Figure 7: Strong and weak scaling for SPARC and ABINIT. The system utilized for strong scaling is  $6 \times 6 \times 6$  FCC unit cells of aluminum with a vacancy. The systems employed for weak scaling are  $3 \times 3 \times 3$ ,  $4 \times 4 \times 4$ ,  $5 \times 5 \times 5$ ,  $6 \times 6 \times 6$ , and  $7 \times 7 \times 7$  unit cells of aluminum, each with a vacancy.

Finally, we compare the minimum wall time achievable by SPARC and ABINIT for the aforementioned aluminum systems. We restrict the maximum number of electrons per core to 96. In SPARC, we choose the number of cores as multiples of 32, whereas we select the number of cores and parallelization scheme in ABINIT that it suggests are optimal. In Table 1, we present the results for the minimum wall time so achieved. We observe that SPARC outperforms ABINIT by factors larger than 1.8 for all the systems considered. In particular, SPARC requires a factor of approximately 4 less wall time for the largest system. Overall, we conclude that SPARC is a highly efficient DFT formulation and implementation that is very competitive with currently existing highly optimized plane-wave codes.

| System                | SPARC        | ABINIT       |
|-----------------------|--------------|--------------|
| $3 \times 3 \times 3$ | 0.95 (64)    | 1.77 (188)   |
| $4 \times 4 \times 4$ | 2.58 (96)    | 5.67 (320)   |
| $5 \times 5 \times 5$ | 9.24 (192)   | 17.42 (396)  |
| $6 \times 6 \times 6$ | 29.42 (384)  | 113.87 (480) |
| $7 \times 7 \times 7$ | 101.80 (576) | 398.77 (795) |

Table 1: Minimum wall time in minutes for  $n \times n \times n$  FCC unit cells of aluminum with a vacancy. The number in brackets denotes the number of cores on which the minimum wall time is achieved.

## 5. Concluding Remarks

In this work, we have developed an accurate and efficient finite-difference formulation and parallel implementation of Density Functional Theory (DFT) for periodic systems, which forms the second component of SPARC (Simulation Package for Ab-initio Real-space Calculations). Specifically, utilizing the Chebyshev polynomial filtered self-consistent field iteration in combination with the reformulation of the electrostatics and the non-local atomic force component, we have developed a framework that enables the efficient evaluation of energies and atomic forces to within chemical accuracies while employing the finite-difference repre-

sentation. Using a wide variety of materials systems, we have demonstrated that SPARC obtains systematic and high rates of convergence in the energy and forces with mesh-size to reference plane-wave results; energy and forces that are consistent and have negligible ‘egg-box’ effect; and accurate ground-state properties. We have also shown that SPARC displays weak and strong scaling that is similar to well-established and optimized plane-wave codes for systems having up to thousands of electrons, but with a significantly smaller prefactor.

There is potential for significant improvement in the efficiency of the current SPARC implementation. In particular, solution of the subspace eigenvalue problem is expected to become the dominant cost for systems consisting of tens of thousands of electrons. Therefore, efficient and parallel scalable eigendecomposition techniques are currently being incorporated into SPARC. Additionally, due to its special outer-product form, a matrix-free approach for the non-local pseudopotential is likely to result in enhanced efficiency and scalability. These improvements along with additional optimization of code are expected to further improve the efficiency of SPARC.

## Acknowledgements

The authors gratefully acknowledge the support of National Science Foundation under Grant Number 1333500.

## References

- [1] P. Hohenberg, W. Kohn, *Physical Review* 136 (1964) B864–B871.
- [2] W. Kohn, L. J. Sham, *Physical Review* 140 (1965) A1133–A1138.
- [3] R. O. Jones, O. Gunnarsson, *Reviews of Modern Physics* 61 (1989) 689.
- [4] T. Ziegler, *Chemical Reviews* 91 (1991) 651–667.
- [5] W. Kohn, A. D. Becke, R. G. Parr, *The Journal of Physical Chemistry* 100 (1996) 12974–12980.
- [6] R. O. Jones, *Reviews of modern physics* 87 (2015) 897.
- [7] G. Kresse, J. Furthmüller, *Physical Review B* 54 (1996) 11169–11186.
- [8] M. D. Segall, P. J. D. Lindan, M. J. Probert, C. J. Pickard, P. J. Hasnip, S. J. Clark, M. C. Payne, *Journal of Physics: Condensed Matter* 14 (2002) 2717–2744.
- [9] X. Gonze, J. M. Beuken, R. Caracas, F. Detraux, M. Fuchs, G. M. Rignanese, L. Sindic, M. Verstraete, G. Zerah, F. Jollet, M. Torrent, A. Roy, M. Mikami, P. Ghosez, J. Y. Raty, D. C. Allan, *Computational Materials Science* 25 (2002) 478–492(15).
- [10] P. Giannozzi, S. Baroni, N. Bonini, M. Calandra, R. Car, C. Cavazzoni, D. Ceresoli, G. L. Chiarotti, M. Cococcioni, I. Dabo, A. Dal Corso, S. de Gironcoli, S. Fabris, G. Fratesi, R. Gebauer, U. Gerstmann, C. Gougaoussis, A. Kokalj, M. Lazzeri, L. Martin-Samos, N. Marzari, F. Mauri, R. Mazzarello, S. Paolini, A. Pasquarello, L. Paulatto, C. Sbraccia, S. Scandolo, G. Sclauzero, A. P. Seitsonen, A. Smogunov, P. Umari, R. M. Wentzcovitch, *Journal of Physics: Condensed Matter* 21 (2009) 395502 (19pp).
- [11] S. Ismail-Beigi, T. A. Arias, *Computer Physics Communications* 128 (2000) 1 – 45.

- [12] F. Gygi, IBM Journal of Research and Development 52 (2008) 137–144.
- [13] J. Cooley, J. Tukey, Mathematics of Computation 19 (1965) 297.
- [14] M. C. Payne, M. P. Teter, D. C. Allan, T. Arias, J. Joannopoulos, Reviews of Modern Physics 64 (1992) 1045–1097.
- [15] J. Hutter, H. P. Lüthi, M. Parrinello, Computational Materials Science 2 (1994) 244–248.
- [16] C. Freysoldt, J. Neugebauer, C. G. Van de Walle, Physical review letters 102 (2009) 016402.
- [17] M. Probert, M. Payne, Physical Review B 67 (2003) 075204.
- [18] P. Suryanarayana, K. Bhattacharya, M. Ortiz, Journal of the Mechanics and Physics of Solids 61 (2013) 38 – 60.
- [19] F. Bottin, S. Leroux, A. Knyazev, G. Zérah, Computational Materials Science 42 (2008) 329–336.
- [20] M. E. Tuckerman, D. Yarne, S. O. Samuelson, A. L. Hughes, G. J. Martyna, Computer Physics Communications 128 (2000) 333–376.
- [21] S. Goedecker, Rev. Mod. Phys. 71 (1999) 1085–1123.
- [22] D. R. Bowler, T. Miyazaki, Reports on Progress in Physics 75 (2012) 036503.
- [23] J. R. Chelikowsky, N. Troullier, Y. Saad, Physical review letters 72 (1994) 1240.
- [24] A. Castro, H. Appel, M. Oliveira, C. A. Rozzi, X. Andrade, F. Lorenzen, M. A. L. Marques, E. K. U. Gross, A. Rubio, Physica Status Solidi B-Basic Solid State Physics 243 (2006) 2465–2488.
- [25] E. Briggs, D. Sullivan, J. Bernholc, Physical Review B 54 (1996) 14362.
- [26] J.-L. Fattebert, Journal of Computational Physics 149 (1999) 75–94.
- [27] F. Shimojo, R. K. Kalia, A. Nakano, P. Vashishta, Computer Physics Communications 140 (2001) 303–314.
- [28] J. E. Pask, B. M. Klein, C. Y. Fong, P. A. Sterne, Physical Review B 59 (1999) 12352–12358.
- [29] S. R. White, J. W. Wilkins, M. P. Teter, Physical Review B 39 (1989) 5819.
- [30] E. Tsuchida, M. Tsukada, Physical Review B 52 (1995) 5573.
- [31] P. Suryanarayana, V. Gavini, T. Blesgen, K. Bhattacharya, M. Ortiz, Journal of the Mechanics and Physics of Solids 58 (2010) 256 – 280.
- [32] P. Motamarri, M. Iyer, J. Knap, V. Gavini, Journal of Computational Physics 231 (2012) 6596–6621.
- [33] J. Fang, X. Gao, A. Zhou, Journal of Computational Physics 231 (2012) 3166–3180.
- [34] T. A. Arias, Reviews of Modern Physics 71 (1999) 267.
- [35] K. Cho, T. Arias, J. Joannopoulos, P. K. Lam, Physical Review Letters 71 (1993) 1808.

[36] L. Genovese, A. Neelov, S. Goedecker, T. Deutsch, S. A. Ghasemi, A. Willand, D. Caliste, O. Zilberman, M. Rayson, A. Bergman, et al., *The Journal of chemical physics* 129 (2008) 014109.

[37] C.-K. Skylaris, P. D. Haynes, A. A. Mostofi, M. C. Payne, *The Journal of Chemical Physics* 122 (2005) 084119.

[38] D. R. Bowler, R. Choudhury, M. J. Gillan, T. Miyazaki, *physica status solidi (b)* 243 (2006) 989–1000.

[39] A. Masud, R. Kannan, *Computer Methods in Applied Mechanics and Engineering* 241 (2012) 112–127.

[40] P. Suryanarayana, K. Bhattacharya, M. Ortiz, *Journal of Computational Physics* 230 (2011) 5226 – 5238.

[41] T. Ono, M. Heide, N. Atodiresei, P. Baumeister, S. Tsukamoto, S. Blügel, *Physical Review B* 82 (2010) 205115.

[42] N. S. Bobbitt, G. Schofield, C. Lena, J. R. Chelikowsky, *Phys. Chem. Chem. Phys.* (2015). DOI: 10.1039/c5cp02561c.

[43] S. Ghosh, P. Suryanarayana, Submitted to *Computer Physics Communications* (2016).

[44] L. Kleinman, D. Bylander, *Physical Review Letters* 48 (1982) 1425.

[45] J. E. Pask, P. A. Sterne, *Phys. Rev. B* 71 (2005) 113101.

[46] S. Ghosh, P. Suryanarayana, *Journal of Computational Physics* 307 (2016) 634 – 652.

[47] F. Bloch, *Zeitschrift für physik* 52 (1929) 555–600.

[48] J. C. Slater, *The self-consistent field for molecules and solids*, volume 4, McGraw-Hill New York, 1974.

[49] H.-r. Fang, Y. Saad, *Numerical Linear Algebra with Applications* 16 (2009) 197–221.

[50] L. Lin, C. Yang, *SIAM Journal on Scientific Computing* 35 (2013) S277–S298.

[51] P. P. Pratapa, P. Suryanarayana, *Chemical Physics Letters* 635 (2015) 69–74.

[52] A. S. Banerjee, P. Suryanarayana, J. E. Pask, *Chemical Physics Letters* 647 (2016) 31 – 35.

[53] J. Harris, *Physical Review B* 31 (1985) 1770.

[54] W. M. C. Foulkes, R. Haydock, *Physical review B* 39 (1989) 12520.

[55] P. Suryanarayana, D. Phanish, *Journal of Computational Physics* 275 (2014) 524 – 538.

[56] K. Hirose, T. Ono, Y. Fujimoto, S. Tsukamoto, *First-principles calculations in real-space formalism*, 2005.

[57] P. P. Pratapa, P. Suryanarayana, J. E. Pask, *Computer Physics Communications* (2015).

[58] S. Balay, J. Brown, , K. Buschelman, V. Eijkhout, W. D. Gropp, D. Kaushik, M. G. Knepley, L. C. McInnes, B. F. Smith, H. Zhang, PETSc Users Manual, Technical Report ANL-95/11 - Revision 3.4, Argonne National Laboratory, 2013.

[59] S. Balay, W. D. Gropp, L. C. McInnes, B. F. Smith, in: E. Arge, A. M. Bruaset, H. P. Langtangen (Eds.), *Modern Software Tools in Scientific Computing*, Birkhäuser Press, 1997, pp. 163–202.

[60] D. A. Mazziotti, *Chemical physics letters* 299 (1999) 473–480.

[61] J. H. Ahlberg, E. N. Nilson, J. L. Walsh, *Mathematics in Science and Engineering*, New York: Academic Press, 1967 1 (1967).

[62] Y. Zhou, Y. Saad, M. L. Tiago, J. R. Chelikowsky, *Journal of Computational Physics* 219 (2006) 172–184.

[63] Y. Zhou, Y. Saad, M. L. Tiago, J. R. Chelikowsky, *Physical Review E* 74 (2006) 066704.

[64] A. V. Knyazev, *SIAM journal on scientific computing* 23 (2001) 517–541.

[65] Y. Zhou, J. R. Chelikowsky, Y. Saad, *Journal of Computational Physics* 274 (2014) 770–782.

[66] J. P. Perdew, Y. Wang, *Physical Review B* 45 (1992) 13244.

[67] D. M. Ceperley, B. J. Alder, *Phys. Rev. Lett.* 45 (1980) 566–569.

[68] N. Troullier, J. L. Martins, *Physical Review B* 43 (1991) 1993–2006.

[69] H. J. Monkhorst, J. D. Pack, *Physical Review B* 13 (1976) 5188.

[70] G. H. Golub, C. F. Van Loan, *Matrix computations*, volume 3, JHU Press, 2012.

[71] C. C. Paige, M. A. Saunders, *SIAM journal on numerical analysis* 12 (1975) 617–629.

[72] C. Lanczos, *An iteration method for the solution of the eigenvalue problem of linear differential and integral operators*, United States Governm. Press Office, 1950.

[73] E. Anderson, Z. Bai, C. Bischof, S. Blackford, J. Demmel, J. Dongarra, J. Du Croz, A. Greenbaum, S. Hammarling, A. McKenney, D. Sorensen, *LAPACK Users' Guide*, Society for Industrial and Applied Mathematics, Philadelphia, PA, third edition, 1999.

[74] D. S. Watkins, *Fundamentals of matrix computations*, volume 64, John Wiley & Sons, 2004.

[75] W. H. Press, *Numerical recipes 3rd edition: The art of scientific computing*, Cambridge university press, 2007.

[76] D. G. Anderson, *Journal of the ACM (JACM)* 12 (1965) 547–560.

[77] J. R. Shewchuk, *An introduction to the conjugate gradient method without the agonizing pain*, 1994.

[78] X. Gonze, B. Amadon, P.-M. Anglade, J.-M. Beuken, F. Bottin, P. Boulanger, F. Bruneval, D. Caliste, R. Caracas, M. Cote, et al., *Computer Physics Communications* 180 (2009) 2582–2615.

[79] X. Gonze, *Zeitschrift für Kristallographie* 220 (2005) 558–562.

- [80] T. Ono, K. Hirose, Phys. Rev. Lett. 82 (1999) 5016–5019.
- [81] V. Brázdová, D. R. Bowler, Atomistic computer simulations: a practical guide, John Wiley & Sons, 2013.
- [82] M. Gillan, Journal of Physics: Condensed Matter 1 (1989) 689.
- [83] D. Marx, J. Hutter, Modern methods and algorithms of quantum chemistry 1 (2000) 301–449.
- [84] J. E. Pask, N. Sukumar, S. E. Mousavi, International Journal for Multiscale Computational Engineering 10 (2012) 83–99.

## Appendix

### A. Electrostatic correction for overlapping pseudocharge densities

In ab-initio calculations, even when the pseudopotential approximation is employed, the repulsive energy is still calculated by treating the nuclei as point charges. Since the electrostatic formulation in this work does not make this distinction, there is disagreement with convention when the pseudocharge densities overlap. The correction which reestablishes agreement can be written as [55]

$$\begin{aligned} E_c(\mathbf{R}) = & \frac{1}{2} \int_{\Omega} \left( \tilde{b}(\mathbf{x}, \mathbf{R}) + b(\mathbf{x}, \mathbf{R}) \right) V_c(\mathbf{x}, \mathbf{R}) \, d\mathbf{x} + \frac{1}{2} \sum_I \int_{\Omega} b_I(\mathbf{x}, \mathbf{R}_I) V_I(\mathbf{x}, \mathbf{R}_I) \, d\mathbf{x} \\ & - \frac{1}{2} \sum_I \int_{\Omega} \tilde{b}_I(\mathbf{x}, \mathbf{R}_I) \tilde{V}_I(\mathbf{x}, \mathbf{R}_I) \, d\mathbf{x}, \end{aligned} \quad (44)$$

where the summation index  $I$  runs over all atoms in  $\mathbb{R}^3$ , and  $V_c(\mathbf{x}, \mathbf{R})$  is the solution of the Poisson equation

$$\frac{-1}{4\pi} \nabla^2 V_c(\mathbf{x}, \mathbf{R}) = \tilde{b}(\mathbf{x}, \mathbf{R}) - b(\mathbf{x}, \mathbf{R}). \quad (45)$$

In addition,  $\tilde{b}$  denotes the reference pseudocharge density, and  $\tilde{b}_I$  represents the spherically symmetric and compactly supported reference charge density of the  $I^{th}$  nucleus that generates the potential  $\tilde{V}_I$ , i.e.,

$$\tilde{b}(\mathbf{x}, \mathbf{R}) = \sum_I \tilde{b}_I(\mathbf{x}, \mathbf{R}_I), \quad \tilde{b}_I(\mathbf{x}, \mathbf{R}_I) = -\frac{1}{4\pi} \nabla^2 \tilde{V}_I(\mathbf{x}, \mathbf{R}_I), \quad (46)$$

$$\int_{\Omega} \tilde{b}(\mathbf{x}, \mathbf{R}) \, d\mathbf{x} = -N_e, \quad \int_{\mathbb{R}^3} \tilde{b}_I(\mathbf{x}, \mathbf{R}_I) \, d\mathbf{x} = Z_I. \quad (47)$$

The discrete form of the repulsive energy correction in Eqn. 44 takes the form

$$E_c^h = \frac{1}{2} h^3 \sum_{i=1}^{n_1} \sum_{j=1}^{n_2} \sum_{k=1}^{n_3} \left( (\tilde{b}^{(i,j,k)} + b^{(i,j,k)}) V_c^{(i,j,k)} + \sum_I b_I^{(i,j,k)} V_I^{(i,j,k)} - \sum_I \tilde{b}_I^{(i,j,k)} \tilde{V}_I^{(i,j,k)} \right), \quad (48)$$

where the integrals have been approximated using the trapezoidal rule in Eqn. 24. The solution of Eqn. 45 is accurate to within a constant, which is determined by evaluating  $\sum_I (V_I(\mathbf{x}, \mathbf{R}_I) - \tilde{V}_I(\mathbf{x}, \mathbf{R}_I))$  at any point in space.

The correction to the atomic forces can be written as [55]

$$\begin{aligned}
\mathbf{f}_{J,c}(\mathbf{R}) = & \frac{1}{2} \sum_{J'} \int_{\Omega} \left[ \nabla \tilde{b}_{J'}(\mathbf{x}, \mathbf{R}_{J'}) \left( V_c(\mathbf{x}, \mathbf{R}) - \tilde{V}_{J'}(\mathbf{x}, \mathbf{R}_{J'}) \right) + \nabla b_{J'}(\mathbf{x}, \mathbf{R}_{J'}) (V_c(\mathbf{x}, \mathbf{R}) + V_{J'}(\mathbf{x}, \mathbf{R}_{J'})) \right. \\
& + \left( \nabla \tilde{V}_{J'}(\mathbf{x}, \mathbf{R}_{J'}) - \nabla V_{J'}(\mathbf{x}, \mathbf{R}_{J'}) \right) \left( \tilde{b}(\mathbf{x}, \mathbf{R}) + b(\mathbf{x}, \mathbf{R}) \right) + b_{J'}(\mathbf{x}, \mathbf{R}_{J'}) \nabla V_{J'}(\mathbf{x}, \mathbf{R}_{J'}) \\
& \left. - \tilde{b}_{J'}(\mathbf{x}, \mathbf{R}_{J'}) \nabla \tilde{V}_{J'}(\mathbf{x}, \mathbf{R}_{J'}) \right] d\mathbf{x}, 
\end{aligned} \quad (49)$$

whose discrete form:

$$\begin{aligned}
\mathbf{f}_{J,c}^h = & \frac{1}{2} h^3 \sum_{J'} \sum_{i=1}^{n_1} \sum_{j=1}^{n_2} \sum_{k=1}^{n_3} \left( \nabla_h \tilde{b}_{J'}|^{(i,j,k)} \left( V_c^{(i,j,k)} - \tilde{V}_{J'}^{(i,j,k)} \right) + \nabla_h b_{J'}|^{(i,j,k)} \left( V_c^{(i,j,k)} + V_{J'}^{(i,j,k)} \right) \right. \\
& + \left. \nabla_h (\tilde{V}_{J'}^{(i,j,k)} - V_{J'}^{(i,j,k)}) \right|^{(i,j,k)} \left( \tilde{b}^{(i,j,k)} + b^{(i,j,k)} \right) + b_{J'}^{(i,j,k)} \nabla_h V_{J'}|^{(i,j,k)} - \tilde{b}_{J'}^{(i,j,k)} \nabla_h \tilde{V}_{J'}|^{(i,j,k)} \right). 
\end{aligned} \quad (50)$$

As before, the summation  $J'$  runs over the  $J^{th}$  atom and its periodic images. For the reference potential, we choose the potential that has been previously employed for generating neutralizing densities in all-electron calculations [84].

## B. Pseudopotential parameters

The cutoff radii  $r_J^c$  employed in this work for the different angular momentum components of the Troullier-Martins pseudopotential are listed in Table 2. The  $l = 0$  component is chosen to be local in all the calculations.

| Atom type | Radial cutoff (Bohr) |         |         |
|-----------|----------------------|---------|---------|
|           | $l = 0$              | $l = 1$ | $l = 2$ |
| H         | 1.25                 | —       | —       |
| Li        | 2.40                 | 2.40    | —       |
| Al        | 2.60                 | 2.60    | —       |
| Si        | 1.80                 | 1.80    | 1.80    |
| Au        | 2.60                 | 2.60    | 2.60    |

Table 2: Cutoff radii for non-local projectors within the Troullier-Martins pseudopotential.

## C. Discrete pseudocharge density properties

The continuous pseudocharge density of the  $J^{th}$  atom has compact support in a sphere of radius  $r_J^c$ —cutoff radius for the local pseudopotential—centered at that atom. However, the corresponding discrete pseudocharge density has infinite extent due to the use of the finite-difference approximated Laplacian. In Fig. 8, for a mesh-size  $h = 0.5$  Bohr, we plot the normalized error in the net enclosed charge as a function of the pseudocharge radius  $r_J^b$ . It is clear that there is exponential decay, which allows for truncation at some finite radius without significant loss of accuracy.

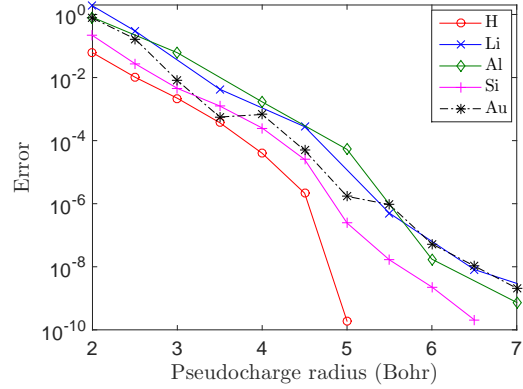


Figure 8: Normalized error in the net enclosed charge as a function of pseudocharge radius for  $h = 0.5$  Bohr.

In Fig. 9, we plot the truncation radius  $r_J^b$  required to achieve the accuracy of  $\varepsilon_b = 10^{-8}$  (Eqn. 28) as a function of mesh-size  $h$ . We observe that  $r_J^b$  becomes smaller as the discretization is refined, with  $r_J^b \rightarrow r_J^c$  as  $h \rightarrow 0$ . The slight non-monotonicity observed at some places in the curves arises due to the fact that  $r_J^b$  is chosen to be a multiple of  $h$  within SPARC.

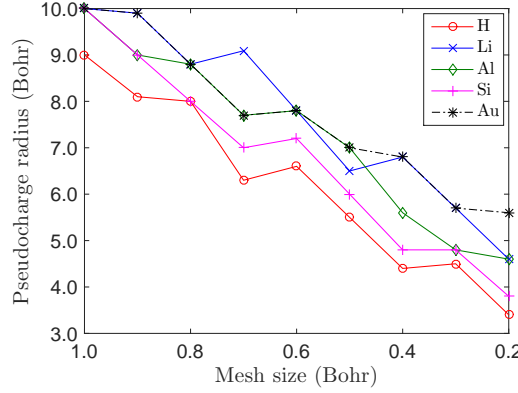


Figure 9: Variation of pseudocharge radius as a function of mesh size.